IEEE Access
Multidisciplinary | Rapid Review | Open Access Journal

Received March 21, 2020, accepted April 16, 2020, date of publication April 29, 2020, date of current version May 15, 2020.

Digital Object Identifier 10.1109/ACCESS.2020.2991298

Impact of a Photodiode's Angular Characteristics on RSS-Based VLP Accuracy

SANDER BASTIAENS[1], WILLEM RAES[2], NOBBY STEVENS[2], (Member, IEEE), LUC MARTENS[1], WOUT JOSEPH[1], (Member, IEEE), AND DAVID PLETS[1], (Member, IEEE)

[1]WAVES Research Group, Department of Information Technology, Ghent University/imec, 9052 Ghent, Belgium
[2]DRAMCO Research Group, ESAT, Department of Electrical Engineering, KU Leuven, 9000 Ghent, Belgium

Corresponding author: Sander Bastiaens (sander.bastiaens@ugent.be)

This work was executed within LEDsTrack, a research project bringing together academic researchers and industry partners. The LEDsTrack project was co-financed by imec (iMinds) and received project support from Flanders Innovation & Entrepreneurship.

ABSTRACT Photodiode (PD)-based Visible Light Positioning (VLP)-based localisation systems seem propitious for the low-cost tracking and route-configurable navigation of automated guided vehicles, found in warehouse settings. Delivering the required high accuracy, currently necessitates measuring and fitting the received power - distance relation. This paper shows that accurately modelling the PD receiver's angular characteristics obsoletes this calibrating fit, while still providing accurate positioning estimates. A new responsivity model *Square (SQ)* is proposed, which is a function of the square of the incidence angle rather than its cosine. Both its aptitude in matching real-life propagation and its associated localisation accuracy are verified using two extensive measurement sets, each detailing the propagation of a PD moving across a 2D plane 3 m below a 4-LED plane. *SQ* is compared to the responsivity and calibration fit models available in the literature. In conjunction with model-based fingerprinting positioning, *SQ* outscores the Lambertian and generalised Lambertian model in terms of the 90th percentile root-mean-square error (rMSE) p_{90} by 45.36 cm (83.1%) and 0.84 cm (8.4%) respectively for the non-Lambertian-like receiver. *SQ* exhibits an equivalent performance as the generalised Lambertian model for the Lambertian-like photodiode. Accounting for the appropriate receiver model can also boost trilateration's rMSE. A 50th percentile rMSE reduction of respectively 1.87 cm and 2.66 cm is found in the setup.

INDEX TERMS Localisation, photodiode, propagation modelling, received signal strength (RSS), receiver, visible light positioning (VLP).

I. INTRODUCTION

A. INDOOR LOCATION TRACKING

The ever-growing degree of automation, particularly in industry, prompts a rapid innovation in indoor localisation. Precise indoor (location) tracking systems should enable a more efficient, more productive and human-safer value chain [1]. A promising indoor tracking application is found in the autonomous 2D navigation of automated guided vehicles (AGVs). Envisioned use cases are e.g. an AGV transporting goods across the factory floor, and an indoor picking robot manoeuvring itself in front of ripe fruit. For highly accurate 2D navigation, most current systems employ either slotted wires embedded in the floor or lasers. Both techniques bring at least one distinct restriction with. The use of slotted wires makes it difficult to dynamically adapt the AGV's routes. Highly-accurate lasers then again add a substantial cost per vehicle and require a reflector infrastructure that is often perceived as disturbing. In addition, recently, the demand for indoor location tracking systems tuned to (miniature) unmanned aerial vehicles (UAVs) has been skyrocketing as well [2].

The associate editor coordinating the review of this manuscript and approving it for publication was Wen Chen.

B. INDOOR LOCALISATION USING VISIBLE LIGHT

New indoor positioning technologies are being evaluated, in an ongoing search for localisation systems that empower low-cost AGVs and UAVs that are self-driving/self-flying along any route. Visible Light Positioning (VLP) might be a well-suited technology for these applications [3].

It employs a photodiode- (PD) or image sensor-based receiver to infer positioning estimates based on the interpretation of signals embedded in the visible light originating from a light-emitting diode (LED) infrastructure. Considering both that LEDs are regarded as the light sources of the future, and that they can simultaneously serve for positioning and illumination, VLP should manage to deliver cost-effective systems. As VLP is also able to deliver outstanding (i.e. sub-decimetre) positioning accuracies [4], the technology allows to reap the benefits of automation with relative ease. Although not yet a mature technology, market intelligence companies, interestingly, already forecast that VLP systems might be the key solutions to unlock the highly-valued indoor location market.

The future will tell whether the dominant VLP system for 2D AGV or 3D UAV tracking will be (smartphone) camera- or photodiode-based. Fact is that both allow accurate positioning. In [5], the authors obtain a post-processed average error of respectively 5.98 cm and 8.68 cm in x and y-direction, when localising a commercial smartphone camera in 82 points underneath a high LED-density setup. Nakazawa *et al.* [6] equipped a 256 by 240 pixels camera with a fish-eye lens in order to achieve a reported minimal horizontal accuracy of 10 cm in a 5.4 m $\times$ 7.5 m $\times$ 3 m room.

However, in applications that are energy- or cost-constrained, but still require a high positioning refresh rate and a significant robustness against stroboscopic or flicker effects (e.g. 3D drone navigation), photodiode-based VLP is favoured. Wang *et al.* [7] proposed to append a PD to a smartphone. Their experiments reported a 90$^{\text{th}}$ percentile root-mean-square error (rMSE) p_{90} of approximately 0.9 m, 1.1 m and 1.8 m in an open-plan office, a cubicle and a corridor environment, respectively. Wang *et al.* do first require performing a set of measurements to fit the *received light intensity* as a function of the LED-receiver distance d.

C. PROBLEM STATEMENT AND RELATED WORKS

Actually, many works on *received signal strength (RSS)*-based VLP necessitate the use of an (arbitrary) calibration fit of the $RSS - d$ relation to provide accurate positioning estimates. The fitting can be either direct via curve fitting [8]–[11] or indirect via machine learning models [12]–[14].

The 16 considered measurement points to test the orthogonal frequency-division multiplexing access (OFDMA)-based quadrature phase-shift keying (QPSK) VLP system proposed in [8], also served as reference points to fit a power law $RSS - d$ relation. In a small-scale setup of 20 cm by 20 cm by 15 cm, a mean positioning error 1.68 cm was achieved. A centimetre order positioning accuracy was also reported by Zheng *et al.* in [9] when localising 36 points in a 1 m by 1.19 m by 1.29 m roll-out, also employing a (Lambertian) power $RSS - d$ relation. Alam *et al.* [10] also remarked the mismatch between measured and modelled $RSS - d$, when employing weighted K-nearest neighbour (WKNN) RSS in a 3.3 m by 2.1 m area with a 2.4 m high ceiling. Utilizing the (Lambertian) power $RSS - d$ fit, with 12 gathered reference points to generate a fingerprint database, only worsens the p_{90} by 0.8 cm. In [11], Alam *et al.* proposed a spring-relaxation (SR)-based positioning method that improves upon the previous WKNN-approach. Armed with the calibration fit, compared to WKNN, a 1.2 cm and 0.8 cm 95$^{\text{th}}$ percentile error improvement is found in respectively the 3.3 m by 2.1 m laboratory and a new 7.5 m by 8 m open foyer environment.

Machine learning methods *fit* the $RSS - d$ relation on a (sparse) collection of training fingerprints. References [12], [13] both ensure accurate localisation using feed-forward neural networks (FNNs). The authors of [12] obtain a factor 7.6 accuracy enhancement with respect to traditional trilateration. Du *et al.* put forward a hybrid approach [14]. To avoid the tedious gathering of a grid of fingerprints, a minimum of 2 reference points serve to fit the power law $RSS - d$ relation. Both the trained 5-hidden layer FNN-based and the trilateration-based 3D localisation then yield approximately the same p_{90} of 12 cm in a 1.2 m $\times$ 1.2 m $\times$ 2 m space. Combining the results of the latter 2 studies [12], [14] implicitly indicates the disparity between the measured and modelled $RSS - d$ relation.

The requirement of directly or indirectly fitting the propagation model is a consequence of an insufficient characterisation of the VLP channel. Furthermore, the $RSS - d$ fit generally increasingly diverges from the $RSS - d$ measurements for larger d, limiting its general applicability.

D. PAPER CONTENT AND STRUCTURE

This paper shows that well-modelling the PD receiver's angular characteristics i.e. *responsivity* or *acceptance* obsoletes this calibrating fit, while still providing accurate trilateration- and model-based fingerprinting (MBF) [15] positioning estimates. Measurements of the receiver's angular dependence for two photodiodes will justify the proposition of a new responsivity model that is a function of the square of the incidence angle rather than its cosine. Extensive measurement sets of the Line-Of-Sight (LOS) propagation of two commercial receivers covering 151^2 points across a 2D plane 3 m below 4 LEDs, allow comparing the performance of a responsivity model with various calibration fit approaches for 2D or 3D trilateration [16] and MBF. While in trilateration, the requirement for an invertible channel model ($RSS - d$) restrains the complexity of the responsivity model, MBF does allow the application of arbitrary models [17]. As such, MBF permits exploring the trade-off in model complexity and positioning performance. A following *simulation* section treats the influence that the shape of the receiver's responsivity has on the positioning accuracy.

The main contributions of this paper can be summarised to:

- An experimental study of a photodiode-based receiver's angular dependency and its impact on the VLP channel and the associated 2D/3D RSS positioning performance.
- The introduction of a new responsivity model, in which a square dependence on the incidence angle is assumed. It is shown that this model obsoletes the calibrating fit

that is often required, and that in conjunction with MBF, accurate 2D localisation is ensured.

This paper extends the receiver acceptance analysis of [17] by performing both additional simulations and single LED experiments in order to verify (and study the parameters of) existing acceptance models. Moreover, new models are proposed that are better suited for (trilateration-based) RSS VLP, and the impact of the receiver's responsivity on the 2D and 3D positioning accuracy is reported for the first time.

The subsequent parts of this paper are grouped in 3 sections. Section II describes the background of, and the materials and methods used throughout the work. Sections II-A to II-E describe respectively the VLP channel model, the available and newly proposed receiver responsivity/acceptance models and the calibrating fits, the positioning algorithms and the measurement setup used. Section III discusses the work's results. Section III-A discusses the result of the propagation measurements performed with both commercial receivers. It looks at how well the treated propagation models, associated with the responsivity and fit models, match with the measured channel. Section III-B builds on Section III-A by now considering the positioning performance of both receivers in LOS conditions. Section III-C discusses the short simulation study on the responsivity shape. Finally, Section IV lists the most important conclusions, and denotes the future work.

II. MATERIALS AND METHODS

A. CHANNEL MODELLING

Presently, the most used VLP channel models in literature still remain the IR-propagation models of Kahn and Barry [18]. Supposing the channel to both have a flat frequency characteristic and be time-invariant stationary, the LOS propagation between a PD and K incoherent white chip-on-board (COB) LEDs LED_i, $i = 1 \ldots K$ can be described using a DC channel gain $h_c^{(i)}$. $h_c^{(i)}$ relates the *received radiant flux/power* P_R at the photodiode to the *transmitted radiant flux/power* $P_{t,i}$ of the LED, via:

$$P_R = \sum_{i=1}^{K} P_{R,i} = \sum_{i=1}^{K} P_{t,i}\, h_c^{(i)}, \quad \text{with}$$
$$h_c^{(i)} = R_E(\phi_i, \gamma_i) \cdot \frac{A_R \cdot \widetilde{R_P}(\psi_i)}{d_i^2} \cdot T_S(\psi_i) \cdot T_R(\psi_i) \qquad (1)$$

where $P_{R,i}$ are demultiplexable using appropriate (de)modulation techniques [19], [20] and where $h_c^{(i)} = 0$, $\psi_i > \psi_C$. In (1), d_i, A_R, ψ_C, ψ_i, γ_i, ϕ_i, $R_E(\phi_i, \gamma_i)$ denote respectively the LED-PD distance, the PD's active area, the receiver field of view, the incidence angle from LED_i, the azimuth angle of irradiance in the horizontal LED plane, the irradiance angle and LED_i's radiation pattern. As approximately-point source LEDs are generally assumed to be ideal Lambertian radiators (of order $m_i = 1$): $R_E(\phi_i, \gamma_i) = R_E(\phi_i) = \left[\frac{m_i+1}{2\pi} cos^{m_i}(\phi_i)\right]_{m_i=1}$. If the PD receiver can be approximated to exhibit Lambertian behaviour with order m_R: $\widetilde{R_P}(\psi) = cos^{m_R}(\psi)$, with m_R often equal to 1. $T_S(\psi)$ and $T_R(\psi)$ represent the receiver's optical filter and concentrator gain respectively.

In [21], Miramirkhani *et al.* described the discrepancies between IR and VL propagation. Cossu *et al.* in [22] showed that the $\widetilde{R_P}(\psi)$ of the photodiode under consideration (Hamamatsu's C5331-11) started diverging from $cos^{m_R}(\psi)$ for $|\psi| > 55°$, when nor a filter nor a lens were used ($T_S(\psi) = T_R(\psi) = 1$). As a result, new or addendum models have been published. In [23], Kim *et al.* propose to generalise the $R_E(\phi_i)$, $\widetilde{R_P}(\psi_i)$, $T_S(\psi_i)$ and $T_R(\psi_i)$ contributions, so that $P_{R,i}$ satisfies:

$$P_{R,i} = \frac{P_{t,i}}{d_i^2}\, C_{opt,i}\, G_t(\phi_i)\, G_R(\psi_i) \qquad (2)$$

$C_{opt,i}$ is the optical power constant (absorbing the influence of A_R and $R_E(0)$), while $G_t(\phi)$ and $G_R(\psi)$ denote the transmitter and receiver gain dependencies. When $G_t(\phi) = \cos^{m_t}(\phi)$ and $G_R(\psi) = \cos^{m_R}(\psi)$, (2) reduces to (1) and can be interpreted as a generalised Lambertian propagation model.

Kim *et al.* [23] also proposed a more general form for $G_t(\phi)$ and $G_R(\psi)$:

$$G_t(\phi) = exp\left(-\phi^{S_t}/k_t\right), \quad k_t = \frac{(\phi_{1/2})^{S_t}}{\ln(2)}$$
$$G_R(\psi) = exp\left(-\psi^{S_R}/k_R\right), \quad k_R = \frac{(\psi_{1/2})^{S_R}}{\ln(2)} \qquad (3)$$

$G_t(\phi)$ and $G_R(\psi)$ are now a function of a slope constant (S_t/S_R for the LED/PD lens respectively) and a semi-angle ($\phi_{1/2}$ and $\psi_{1/2}$ for the LED/PD respectively).

$R_P(\psi)$ collects the ψ-dependencies and is dubbed the *angular acceptance* or *normalised responsivity*: $R_P(\psi) = T_S(\psi) \cdot T_R(\psi) \cdot \widetilde{R_P}(\psi)$ in (1) and $R_P(\psi) = G_R(\psi)$ in (2).

B. ANGULAR ACCEPTANCE/RESPONSIVITY MODELS

In response to incident light, the PD generates photocurrent contributions $\{I_{PD,i}\}$. The observed $\{P_{R,i}\}$ values are related to $\{I_{PD,i}\}$ by means of the photodiode's nominal responsivity $\widehat{R_P}(P_{R,i})$:

$$P_{R,i} = \frac{I_{PD,i}}{M \cdot \widehat{R_P}(P_{R,i})} \qquad (4)$$

As reverse-biased PIN PDs have an extremely linear $P_{R,i} - I_{PD,i}$ response, while $P_{R,i}$ is below saturation, $\widehat{R_P}(P_{R,i})$ can be assumed to be independent of $P_{R,i}$: $\widehat{R_P}(P_{R,i}) = \mathbf{R_P}(0)$. A gain mismatch factor M is introduced to account for the wavelength λ mismatch between transmitter ($R_E(0)$) and receiver ($\mathbf{R_P}(0)$). M ensures that a wavelength λ-abstracted channel model approach remains valid. In this paper, all receiver dependencies (exempt A_R) are collected in the term *responsivity* $\mathbf{R_P}(\psi)$, with $\mathbf{R_P}(\psi) = \mathbf{R_P}(0) \cdot R_P(\psi)$.

This paper focusses solely on the impact of $R_P(\psi)$ on the 2D/3D RSS VLP's positioning performance. Obviously, $R_P(\psi)$ is derived from $\mathbf{R_P}(\psi)$ by division by the maximum responsivity $\mathbf{R_P}(0)$.

Based on Section II-A, the following $R_P(\psi)$ models can be identified: (a) the standard Lambertian

model $R_P(\psi) = \cos(\psi)$ with acronym $m = 1$, (b) the generalised Lambertian model $R_P(\psi) = \cos^{m_R}(\psi)$ denoted by m_R, (c) the exponential model $R_P(\psi)$ (see (3)) dubbed *Exp*. In $m = 1$ and m_R, $T_S(\psi)$ and $T_R(\psi)$ are equal to 1 as both the LEDs and the PD are not explicitly equipped with a lens. Technically, *Exp*, also describes a lens, but is here considered as a ψ dependence.

This paper also proposes (d) a new quadratic $R_P(\psi)$ model, denoted as *Square* (*SQ*) and presented in (5).

$$R_P(\psi) = \begin{cases} 1 - \dfrac{\psi^2}{(\psi_{3dB})^2} \cdot \dfrac{\sqrt{2}-1}{\sqrt{2}}, & |\psi| \leq |\psi_C| \\ 0, & |\psi| > |\psi_C| \end{cases} \quad (5)$$

in which ψ_{3dB} represents the ψ for which $R_P(\psi) = 1/\sqrt{2}$ (i.e. a 3 dB electrical power decrease). $|\psi_C|$ is the minimum of the receiver field of view (FOV) and $\sqrt{\sqrt{2}\,\psi_{3dB}^2/\left(\sqrt{2}-1\right)}$. *SQ* displays a steeper $R_P(\psi)$ gradient when ψ approaches $|\psi_C|$ as to better cope with the $cos^{m_R}(\psi)$ model's divergence for $|\psi| > 55°$. *SQ* is noninvertible, which will hinder straightforward application in trilateration-based positioning (see hereinbelow in Section II-D2). Therefore, an approximated (e) SQ_{approx} $R_P(\psi)$ model is proposed:

$$R_P(\psi) = \begin{cases} 1 - \dfrac{(2-\sqrt{2})(1-\cos(\psi))}{(\psi_{3dB})^2}, & |\psi| \leq |\psi'_C| \\ 0, & |\psi| > |\psi'_C| \end{cases} \quad (6)$$

with $|\psi'_C|$ the minimum of the receiver field of view (FOV) and $\text{acos}\left(1 - \psi_{3dB}^2/\left(2-\sqrt{2}\right)\right)$.

Importantly, all treated $R_P(\psi)$ models are LED independent and the photodiode is operating in overfill condition as is expected in optical wireless. Each of the 5 $R_P(\psi)$ models' aptitude in matching the measured $R_P(\psi)$ behaviour will be evaluated in Section III in terms of the coefficient of determination R^2 (and later the positioning performance).

C. CALIBRATING FITS OF THE CHANNEL MODEL

Ideally, all parameters in the described channel models (see Section II-A) can be predetermined and are constant per LED and receiver type. In practice however, as a consequence of the channel models diverging from real-life measurements due to both variations on the LEDs' radiation pattern and the improper modelling of $R_P(\psi)$ [22], many works in literature calibrate certain channel parameters, often even per LED. Off-line, on-site measurements serve to fit the $P_{R,i} - d$ relation [7]–[10]. In [9], [10], the authors simplify (1) to a power law $P_{R,i} - d_i$ relationship ν_i:

$$P_{R,i} = P_{R,i,0} \cdot \left(\frac{d_{i,0}}{d_i}\right)^{\nu_i} \quad (7)$$

$d_{i,0}$ and $P_{R,i,0}$ denote the calibration distance d_i and received radiant power $P_{R,i}$ respectively. ν_i represents the generalised Lambertian modelling of the LED m and PD ν'_i (i.e. $\nu_i = 2 + m + \nu'_i$). ν_i, see (7), can be generalised to $P_{R,i} = \alpha_i \cdot d_i^{\beta_i}$, which will be referred to by *Power*. Some works even calibrate a seemingly more arbitrary propagation model, e.g. in [7] a second order polynomial fit is worked with. The drawback of 'fitting' lies in the recalibration effort needed when either the LED, the PD or the environment parameters change.

D. POSITIONING

The propagation models of the previous sections can be used to infer positioning, when combined with the algorithms discussed next. The receiver position is denoted by (x_u, y_u, z_u). A prerequisite for accurate positioning is that the LED coordinates $(x_{S,i},\ y_{S,i},\ z_{S,i})$ are meticulously known.

1) MODEL-BASED FINGERPRINTING (MBF)

Model-based fingerprinting RSS VLP employs a precomputed propagation map, accounting for the relevant channel characteristics. It holds the RSS values per LED, i.e. $\{P_{R,i}\}$, for all locations on a predefined positioning grid. Upon a set of $\{P_{R,i}\}$ measurements $\{\widehat{P_{R,i}}\}$, the grid position that has the closest, in terms of rMSE, set of modelled $\{P_{R,i}\}$ values to the measured $\{\widehat{P_{R,i}}\}$ is taken to be the positioning estimate [15]. The additional propagation map dimension needed for (real-time) 3D localisation (whether or not in the presence of receiver tilt) renders MBF infeasible (in terms of latency and the required storage) for e.g. drone localisation.

2) TRILATERATION

a: 2D TRILATERATION

Trilateration-based RSS estimates the distances d_i directly from $P_{R,i}$ by inverting one of the above propagation models. Afterwards, the d_i are translated into a location estimate of (x_u, y_u, z_u) by means of the well-known least-squares matrix formalism (as used in [24]).

The invertible channel model requirement restrains the complexity of the employed $P_{R,i}$ - d_i relation, and thus of the $R_P(\psi)$ model.

b: 3D TRILATERATION

In 3D trilateration, z_u is no longer a priori known and needs to be estimated as well. In this paper, the localisation algorithm of Plets *et al.* is employed. The algorithm performs an iterative evaluation of the 2D procedure of hereinabove and is detailed in [16].

E. MEASUREMENT SETUP

To both characterise $R_P(\psi)$ for two commercial Thorlabs PDs, namely Thorlabs' PDA100A2[1] or PDA36A2,[2] and study the effect of $R_P(\psi)$ on the positioning performance, it is required to use two different measurement setups. The former setup is detailed in Section II-E1, the latter in Section II-E2. Common to both experiments, the considered PD's photocurrents are amplified with a transimpedance gain G_{PD} to photovoltages, which are then N times sampled at a rate f_S using National Instrument's USB-6212 DAQ

[1] https://www.thorlabs.com/thorproduct.cfm?partnumber=PDA100A2
[2] https://www.thorlabs.com/thorproduct.cfm?partnumber=PDA36A2

Device. A MATLAB® backend then processes the measurement. The characteristics of both photodiodes are listed in Table 1. The COB LEDs utilised in the experiments are of the Bridgelux *BXRE-50C3001-D-24*[3] type.

TABLE 1. Comparison of PDA100A2 and PDA36A2. The G_{PD} values reported are employed for positioning.

PDA100A2	PDA36A2
	
Form Factor Round	**Form Factor** Square
Active Area $A_R = 75.4\ \text{mm}^2$	**Active Area** $A_R = 13\ \text{mm}^2$
Gain $G_{PD} = 4.75 \cdot 10^4\ \text{V/A}$	**Gain** $G_{PD} = 4.75 \cdot 10^5\ \text{V/A}$

1) SINGLE LED EXPERIMENT FOR $R_P(\psi)$

Fig. 1 shows the $R_P(\psi)$ measuring setup, consisting of a single LED (highlighted in purple) that looms directly over the centre point of a receiving platform (highlighted in green). This in-house-made platform consists of a linear actuator, moving the tilting structure on top accurately up and down (in the z-direction). The schematic representation of the *tilter* is visualised in Fig. 2. By placing either of the PDs on top of a Thorlabs *GNL*20/*M*[4] goniometer, itself fixed on the *tilter*, ψ can be accurately set. The *GNL*20/*M* fine-grainedly tunes ψ between $[-10°, 10°]$ around a ψ set point determined by the *tilter*. As the *tilter* not only tilts the PD's normal, but also displaces the PD at each *tilter* setting, the receiving platform moves a predefined (according to the laws of trigonometry) distance both vertically and horizontally to keep the PD at the same 3D location. The *tilter* set points are $[-5°, 10°, 25°, 40°, 55°, 70°, 85°]$. The LED-PD distance amounts to 1.25 m. The centre point of the receiving platform coincides with the gravity centre of the PD's active area. G_{PD} here is a tenth of the values of Table 1. The BXRE LED is transmitting DC light in response to a DC driving current magnitude of 750 mA. $f_S = 256$ kHz, $N = 51.2$ kS and 50 photocurrent waveforms are averaged. The obtained $R_P(\psi)$ dataset is referred to as *Point*, as $R_P(\psi)$ is measured for 1 receiver location, underneath the LED.

2) LOCALISATION MEASUREMENT SETUP

The extent of the impact of the normalised responsivity $R_P(\psi)$ models on the VLP channel model quality and the corresponding positioning performance is studied in WAVES' VLP lab [17]. One of either PDs is installed on top of a 2D slider (Velmex' BiSlides) that covers 1 m^2 with a uniform grid of 41^2 points. By sequentially displacing the slider 1 m,

[3]https://www.bridgelux.com/sites/default/files/resource_media/DS43%20V15%20Array%20Data%20Sheet%20Rev%20E%2020160606.pdf

[4]https://www.thorlabs.com/thorproduct.cfm?partnumber=GNL20/M

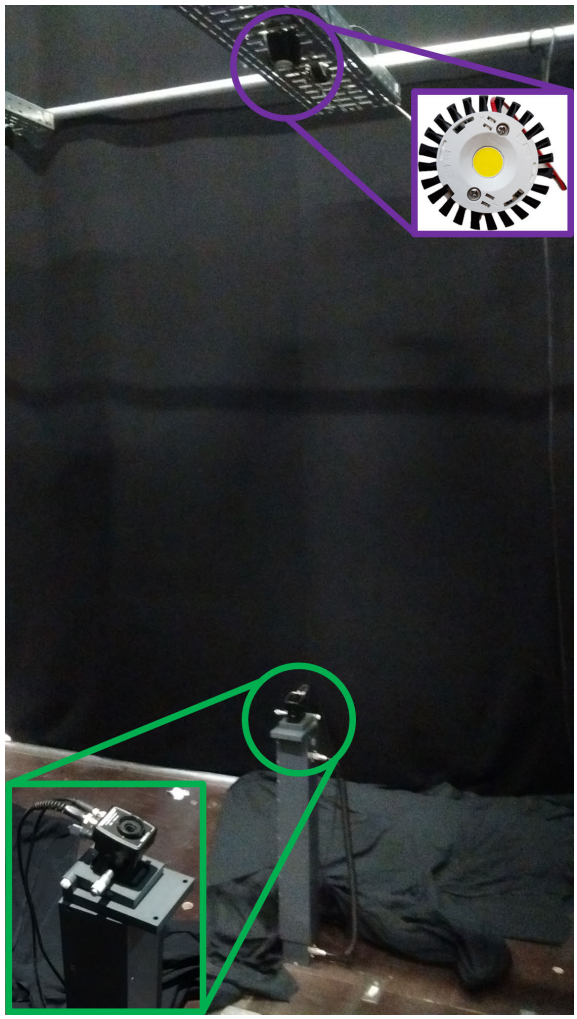

FIGURE 1. Single LED experiment for $R_P(\psi)$. A zoom-in of the receiver/LED setup is indicated in green/purple.

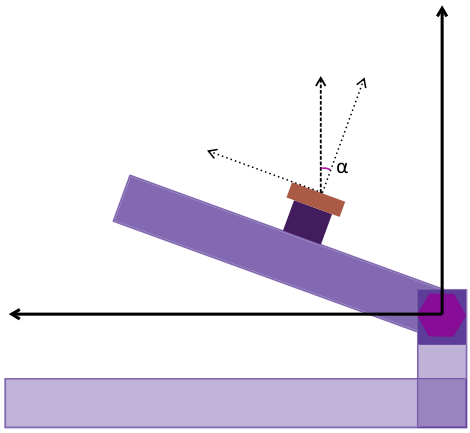

FIGURE 2. Schematic of the tilt platform.

$I_{PD,i}$ can be measured for a 4 m × 4 m ground plane with a granularity of 2.5 cm. The DAQ is configured to sample $N = 150$ times at a rate $f_S = 75$ kHz i.e. to ensure coherent sampling. The MATLAB® backend then performs fast Fourier transform (FFT)-demodulation into $I_{PD,i}$ values

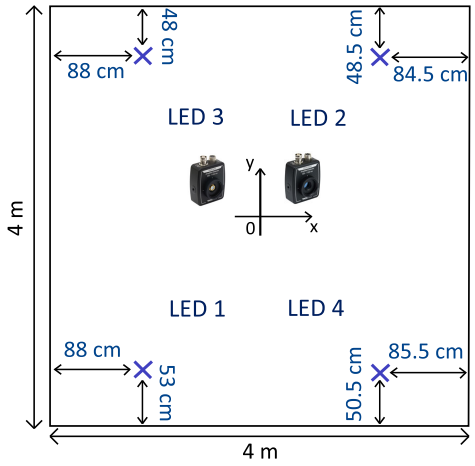

FIGURE 3. Overview of the localisation measurement setup.

as specified in [19]. Per measurement location, 10 $I_{PD,i}$ values are averaged to reduce the noise impact. Fig. 4 depicts the schematic representation of this receiver chain.

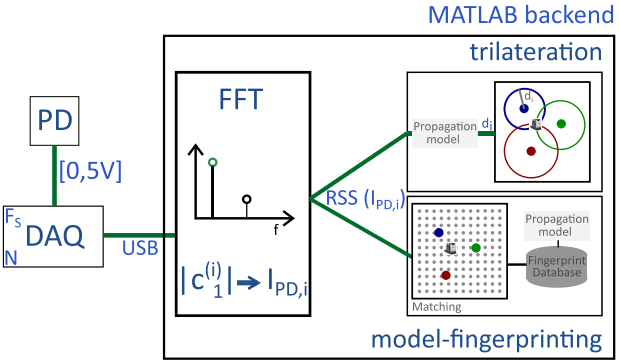

FIGURE 4. Schematic overview of the receiver chain and localisation backend.

At a height of 3 m above the receiver plane, a nearly square-shape LED constellation of ($K = 4$) BXRE COBs is installed. These LEDs are intensity-modulated as to transmit pulse trains (with current magnitudes $\approx$ [600, 750, 750, 750] (mA)) with frequencies $f_{c,i}$ and with duty cycle $\delta_i = 0.5$ [25]. To demultiplex the contributions of the different LEDs at the receiver side, $f_{c,i}$ are chosen to satisfy: $f_{c,i} = 2^{i-1} f_0$ [19]. f_0 is set to 500 Hz to exceed the flicker threshold. The LED coordinates are depicted in Fig. 3, with $\{z_{S,i}\} = [3.005, 3.015, 2.993, 3.004]$ (m). To minimise the influence of multipath, the VLP lab is covered with black cloths as side walls.

a: APPLICATION TO NORMALISED RESPONSIVITY

Rearranging the expression of (1), also allows deriving $R_P(\psi)$ from the $I_{PD,i}$ measurements. The LEDs' measurement data $I_{PD,i}$ is overlaid, compensated by $R_E(\phi_i, \gamma_i)$ and d_i^2, and then per LED normalised. The resulting $R_P(\psi)$ dataset is named *Plane*, as $R_P(\psi)$ is obtained by measuring spatially distributed receiver locations i.e. receiver locations on the ground plane.

III. RESULTS

A. CHANNEL CHARACTERISATION

In order to both model the receivers' (angular) characteristics and study their impact on $I_{PD,i} - d_i$ and thus on the positioning, the propagation is measured across the 2D receiver plane. The receivers' normal n_R is assumed to remain equal to [0 0 1]. The (demodulated) received photocurrents $I_{PD,i}$ are shown in Fig. 5, for LED 3 and respectively the (a) PDA100A2 and (c) PDA36A2.

1) CALIBRATION OF MEASUREMENT SETUP IMPERFECTIONS

To limit the influence of all non-responsivity channel contributions in deriving $R_P(\psi)$ and in the positioning, additional calibration steps are required.

a: RADIATION PATTERN

In trilateration, $R_E(\phi_i, \gamma_i)$ is assumed to be Lambertian (generally with order $m = 1$). Fig. 6 shows by means of the C0, C45 and C90 slices of *BXRE-50C3001-D-24*'s C0/C90 photometric diagram that $R_E(\phi_i, \gamma_i)$ slightly deviates from the best fitting Lambertian radiator with $m = 1.138$, which is depicted in black. During MBF localisation and the derivation of $R_P(\psi)$, the tabulated $R_E(\phi_i, \gamma_i)$ is used.

b: TRANSMITTER TILT

Nonnegligble LED tilts present in the lab setup, arising from manually installing them on rails, need compensation. The most likely LED normal is found where $I_{PD,i} \cdot d_i^3$ is maximal in the receiver plane [26]. A more robust method, accounting for outliers, entails taking the $I_{PD,i} \cdot d_i^3$-weighted centroid of all locations with an $I_{PD,i} \cdot d_i^3$ larger than the 95$^{\text{th}}$ percentile of all $I_{PD,i} \cdot d_i^3$. The centroids are highlighted in red in Fig. 5 (b) and indicate the intersections of the LED normals and the receiver plane. The tilt is then compensated for by sequentially dividing the measurement data $I_{PD,i}$ on each grid location (x, y) by $\cos(\phi_m(x, y))$ and then multiplying it by $\cos(\phi_{id}(x, y)) = {}^{(z_{S,i}-h)}/_{d_i(x,y)}$. $\phi_m(x, y)$ and h represent the measured irradiance angle (with respect to the tilted LED normals $\{n_{S,i}\}$) and the z-coordinate of the PD [17].

c: RADIANT FLUX $P_{t,i}$

$P_{t,i}$ also requires a calibration, as it is never exactly known without measuring [27]. Given M and $\mathbf{R_P}(0)$, $\{P_{t,i}\}$ are calibrated directly beneath each LED after accounting for the transmitter tilt. The calibrated $P_{t,i}$ satisfy approximately $P_{t,1} \cdot [1\ 1.245\ 1.225\ 1.2]$. $P_{t,i}|_{i>1} < 1.25\, P_{t,1}$ can (partly) be attributed to the LED driving current - $P_{t,i}$ relation starting to saturate (see Section II-B). In addition, the variation in $P_{t,i}$ will impede propagation models that assume a LED independent $P_{t,i} = P_t,\ i = 2..K$.

2) NORMALISED RESPONSIVITY $R_P(\psi)$

Fig. 7 depicts the normalised receiver responsivity $R_P(\psi)$ measurements of both Thorlabs receivers, over the incidence angle ψ. A clear disparity in $R_P(\psi)$ between both receivers is

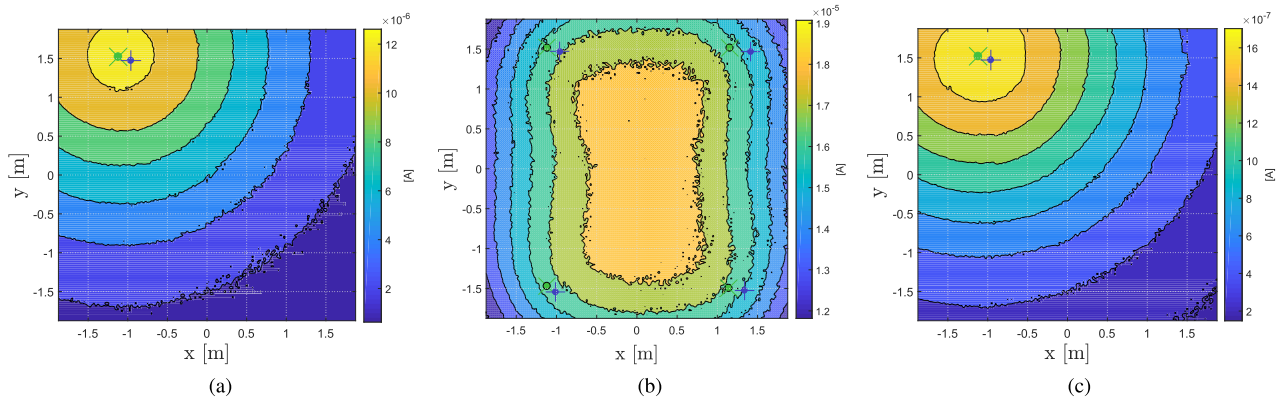

FIGURE 5. Distribution of $I_{PD,3}$ measured with the (a) PDA100A2 and (c) PDA36A2 across the receiving plane. (b) plots PDA100A2's $\sum_{i=1}^{K} I_{PD,i}$, but where all $I_{PD,i}$ are weighted to all have equal $P_{t,i} = P_{t,1}$. The green markers represent the LED locations, whereas the purple markers highlight the points of incidence between the LEDs' surface normals $\{n_{S,i}\}$ and the ground plane.

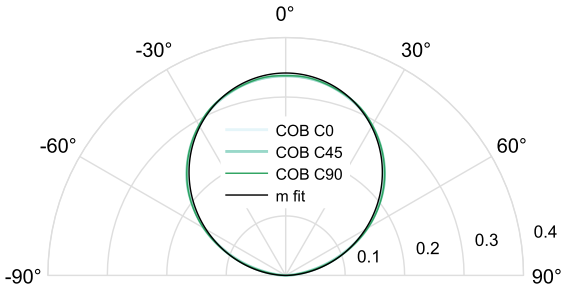

FIGURE 6. Polar representation of the C0, C45 and C90 slice of, and the $m = 1.138$ fit of $R_E(\phi_i, \gamma_i)$.

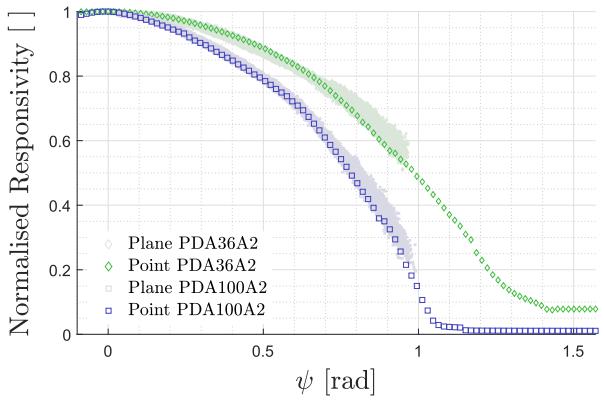

FIGURE 7. $R_P(\psi)$ for the PDA36A2 (green) and PDA100A2 (purple). The *Point* and *Plane* keywords denote the employed measurement setup (see Section II-E). *Point* refers to the *Single LED* setup, where $R_P(\psi)$ is measured by tilting the PD at one location. *Plane* encompasses the $R_P(\psi)$ data that is obtained with the *Localisation Measurement Setup*.

noticed. PDA36A2's $R_P(\psi)$ is depicted in the green shades, PDA100A2's in the purple ones. The lighter and darker shades represent the data from the 2D *Plane* measurement setup (see Section II-E2) and the single LED tilting *Point* setup (Section II-E1) respectively.

a: EXISTING $R_P(\psi)$ MODELS

The $R_P(\psi)$ acceptance models of Section II-B are fit on the *Plane* $R_P(\psi)$ measurement data and are subsequently depicted in Fig. 8. *Plane* is deemed more reliable (than *Point*) due to the manual operation of the *tilter*. It furthermore allows comparing the $R_P(\psi)$ models with the calibrating fits of Section II-C.

(a) The Lambertian $R_P(\psi)$ model $m = 1$ (visualised in light green) yields an R^2 score of 0.99/0.345 for the PDA36A2/PDA100A2. $m = 1$ starts diverging from the measured $R_P(\psi)$ at $\psi > 50°$ and 7.5°.

(b) The generalised Lambertian model dubbed m_R, with fitted $m_R = 0.98/1.9$ visualised in eucalyptus (dark) green, improves R^2 to 0.991/0.986. It particularly fits PDA36A2's $R_P(\psi)$ well. (a) and (b) allow concluding that the PDA36A2 exhibits a rather Lambertian-like responsivity behaviour (i.e. $m_R \sim 1$), while, in contrast, the PDA100A2 does not. PDA100A2' divergence from the ideal Lambertian response can be partly attributed to inherent photodiode physics [28], [29]. However, it is mainly due to additional internal reflections or blockage instilled by the packaging. At large ψ, both $m = 1$ and m_R gradually saturate towards $\psi = \pi/2$. The measured $R_P(\psi)$ noticeably differs by dropping to zero (or equivalently, the noise floor).

(c) *Exp*, the exponential form of $G_R(\psi)$ of (3) shown in orange, identifies $\psi_{1/2}$ to be 1.06/0.80 rad and then fits $S_R = 2.3/2.39$. *Exp*'s consistent fitted parameters and R^2 scores ($R^2 = 0.988/0.987$) entails it being a more robust, universally applicable model. For ψ exceeding 1.3 rad, *Exp* starts diverging more and more from the *Point* measured data. When $R_P(\psi) \approx 1/2$ is inadequately known (see Fig. 8), *Exp* may encounter difficulties. In [17] therefore, a slightly modified model was introduced, which utilises the "three-quarter" angle to deliver comparable R^2 scores.

(d) Rated at $R^2 = 0.991/0.993$, *SQ* exceedingly outperforms the m_R model, certainly at ψ approaching $|\psi_C|$. *SQ* is more able to account for the PDA100A2-receiver's behaviour, due to it having a larger $R_P(\psi)$ gradient when $\psi \to |\psi_C|$. It is displayed in *curious* (darkest) blue. ψ_{3dB} amounts to 0.79 and 0.61 rad respectively. Moreover, no fit is required.

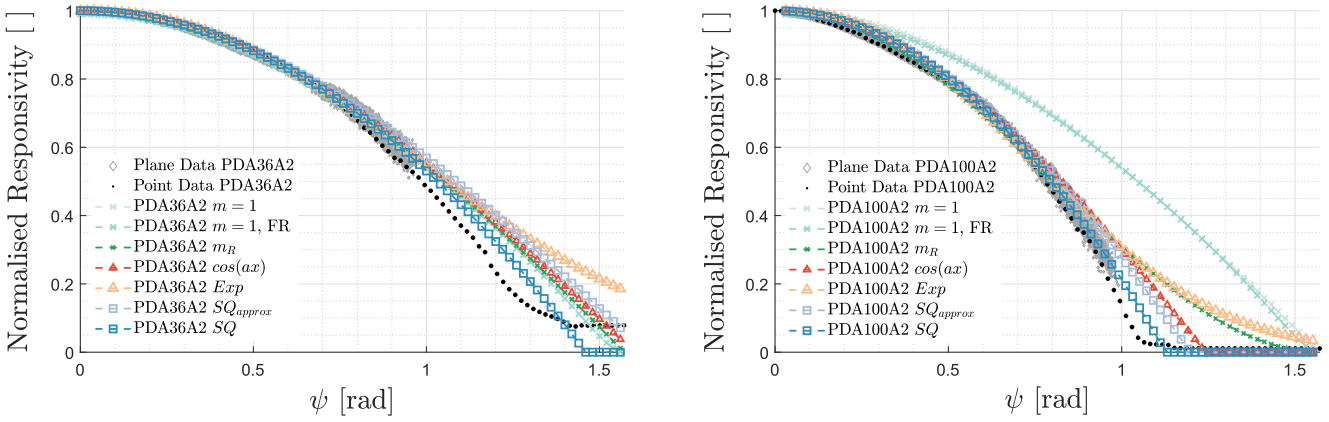

(a) PDA36A2 (b) PDA100A2

FIGURE 8. Angular acceptance measurements and models for (a) the PDA36A2 and (b) the PDA100A2.

(e) The associated SQ_{approx} model, shown in light steel (middle) blue, is seemingly unsuccessful in delivering the high R^2 scores ($R^2 = 0.983/0.982$) required.

b: OTHER $R_P(\psi)$ MODELS

The angular pseudospectrum of the *MUltiple SIgnal Classification (MUSIC)* algorithm [30] with $R_P(\psi)$ as input, shows a single and distinct peak indicating that $R_P(\psi)$ could be modelled by a cosine function $R_P(\psi) = \cos(a \cdot \psi)$. This model is named cos(ax). a is a scaling factor. It is returned by identifying the pseudospectrum peak. cos(ax) is plotted in red and shows that *SQ fits* $R_P(\psi)$ at least as well as an arbitrary cosine function.

It can be remarked that all $R_P(\psi)$ models increasingly diverge from the measured data, for $\psi \sim |\psi_C|$. For *SQ* though, this divergence is mainly restrained to the neighbourhood of $|\psi_C|$ i.e. where $R_P(\psi)$ saturates. At these higher ψ, Fresnel losses manifest itself. Averaging the Fresnel s and p-polarisation equations, allows adding a Fresnel loss contribution to the $R_P(\psi)$ models. The reflection coefficient of silicon (= 4.22) is obtained by weighing the refractive index data of Schinke *et al.* [31] with the BXRE LEDs' wavelength spectrum. Fig. 8 shows the additional Fresnel loss impact (at high ψ) in conjunction with the $m = 1$ model in riptide (middle) green (i.e. the curve denoted with $m = 1$, FR). Adding the Fresnel losses to the *SQ* shifts its infliction point (i.e. $|\psi_C|$) even closer to the actual measured $R_P(\psi)$'s. All models' resulting coefficients of determination are collected in Table 2.

The analysis performed in this section suggests that the *SQ* acceptance model best approximates the measured $R_P(\psi)$. In Section III-B1, the model's goodness of fit is translated into a positioning accuracy.

3) CALIBRATING FITS

The $R_P(\psi)$ models of the previous section are LED independent. As stated in Section II-C, in VLP literature, the propagation models are frequently calibrated per LED.

TABLE 2. Coefficient of determination R^2 of the $R_P(\psi)$ responsivity models.

PDA	$\mathbf{m = 1}$	$\mathbf{m = 1}$, FR	$\mathbf{m_R}$	$cos(\mathbf{ax})$	Exp	$\mathbf{SQ_{approx}}$	SQ
36A2	0.99	0.984	0.991	0.991	0.988	0.989	0.991
100A2	0.345	0.391	0.986	0.983	0.987	0.983	0.993

This subsection effectuates the fitting of the models of Section II-C on the measured received photocurrent $I_{PD,i}$ - distance d_i relation as to ready them for application for positioning. In addition, it is investigated how the *SQ* model fares in comparison with the calibration fits.

Fig. 9 (a) and (b) depict the measured (and tilt-compensated) $I_{PD,1}$ - d_1 (i = 1) relation in grey diamonds for respectively the PDA36A2 and the PDA100A2. Noise, interference and small measurement/setup errors (e.g. imperfectly compensated tilt) cause the curves to widen with increasing inter-PD-LED distance d. 5 calibrated models are considered (see Section II-C) and depicted in Fig. 9: (i) $\nu_i' = 1$, (ii) ν_i tilt, (iii) ν_i, (iv) $\nu_i = \nu$ and (v) *Power*. (i) $\nu_i' = 1$ is the baseline model, in which the LED *and* the PD receiver are assumed to be Lambertian with order 1.138 (see Section III-A1) and order 1 respectively. Its mean R^2 over the 4 LEDs equals for the PDA36A2 and PDA100A2 respectively 0.996/0.965. $\nu_i' = 1$ corresponds to the (a) $m = 1$ $R_P(\psi)$ responsivity model. The (ii) ν_i tilt and (iii) ν_i are generalised models in the sense that they fit a joint exponent containing both receiver and LED ψ dependence (both fit the ν_i exponent in (7)). (ii) ν_i tilt is the only model that fits the uncompensated data. (ii) ν_i tilt and (iii) ν_i both push the R^2 score towards 0.998 for both PDs. The mean ν_i is 4.01/4.87 for the PDA36A2/PDA100A2. In [17], it was shown that propagation models whichever hypothesise $P_{t,i} = P_t$ lead to an inferior $I_{PD,i} - d_i$ fit. Optimising a single ν_i jointly over all LEDs leads to the (iv) $\nu_i = \nu$, which scores comparatively at 0.9978/0.9976 in terms of R^2. The last model *Power* achieves the highest $R^2 = 0.9981/0.9981$. It should deliver a model well-suited for trilateration as d_i is easily gathered from $I_{PD,i}$. *Power* does require to fit 2 degrees of freedom

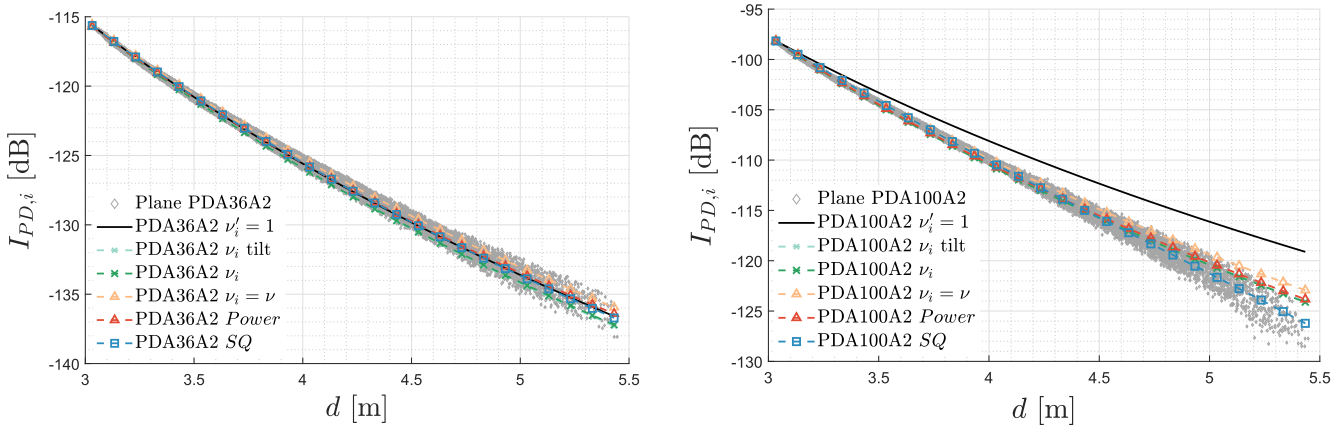

(a) PDA36A2 (b) PDA100A2

FIGURE 9. $I_{PD,1}$ - d_1 and the (fitted) propagation models as found in literature for (a) the PDA36A2 and (b) the PDA100A2.

instead of 1. The parameters are obtained by employing the curve fitting tool *cftool* of MATLAB® (i.e. nonlinear least squares minimisation). The mean exponents $\overline{\beta_i}$ are -3.93 and -4.9 and emphasise the difference between both PDs.

All these calibration model parameters are fit by minimising the rMSE between the modelled and measured data and hence correspond to fitting a practical propagation model in situ [10]. Each model's mean coefficient of determination R^2 with respect to the measurement data is listed in Table 3 for overview. Importantly though, the fitted $I_{PD,i}$ - d_i relations diverge more and more from the measured ones with increasing distance d_i. This behaviour (also treated in the Section III-A2) will, depending on the VLP roll-out situation, significantly impact the positioning accuracy.

TABLE 3. Mean coefficient of determination R^2 of the calibrating fits.

PDA	$\nu_i' = 1$	ν_i tilt	ν_i	$\nu_i = \nu$	Power	SQ $R_P(\psi)$
36A2	0.9963	0.9975	0.9974	0.9978	0.9981	0.9972
100A2	0.9649	0.9976	0.9977	0.9976	0.9981	0.9978

To investigate whether adequately modelling the nominal receiver responsivity will spare the effort of calibration-based fitting, the *SQ* model's associated $I_{PD,1}$-d_1 is plotted in blue in Fig. 9 as well. Fig. 9 demonstrates that *SQ* better approximates the measured behaviour at higher d, due to *SQ* being well-suited for $\psi \rightarrow |\psi_C|$. The R^2 scores slightly diminish however to 0.9972 and 0.9978. As these scores are comparable to the ν_i model's *SQ* should deliver accurate localisation estimates.

B. LOCALISATION PERFORMANCE

This section evaluates the aptitude of the different propagation models of the previous section in terms of their associated positioning accuracy found in the VLP roll-out configuration (Section II-E2). Section III-B1 treats model-based fingerprinting (MBF) localisation, whilst Section III-B2 details the trilateration-based positioning results.

1) MODEL-BASED FINGERPRINTING (MBF)

MBF's propagation map has a 1 cm grid resolution and accounts for the *BXRE-50C3001-D-24*s' tabulated $R_E(\phi, \gamma)$ and the measured tilt normal. The 3 strongest LEDs, in terms of $I_{PD,i}/P_{t,i}$, are used in the positioning process (as this performs better), inadvertently limiting the maximal ψ_i found at the receiver. Part of MBF's benefit is that it can account for arbitrary and/or irregular propagation models, arising from arbitrary LED radiation and PD normalised responsivity patterns.

a: MBF AND $R_P(\psi)$

Fig. 10 shows the cumulative distribution (CDF) of the rMSE found during MBF localisation associated with the $R_P(\psi)$ models of Section III-A2. In addition, Table 4 shows the 50$^{\text{th}}$ percentile p_{50}, the 75$^{\text{th}}$ percentile p_{75} and the 90$^{\text{th}}$ percentile p_{90} rMSE.

The black curve CDF substantiates the hypothesis of Section III-A2 in that the baseline $m = 1$ model is unable to supply sufficient localisation accuracy for both Lambertian-like (with $p_{50} = 5.85$ cm) and non-Lambertian-like photodiode receivers (with $p_{50} = 33.97$ cm). m_R significantly improves upon $m = 1$ and shifts $m = 1$ over approximately 30 mm for the PDA36A2 and 82% for the PDA100A2 (see the eucalyptus (dark) green curve). Although [23] showed the rationale for *Exp* (displayed in orange), this work finds m_R to outscore *Exp*. The remark has to be made though that the respective photodiodes are not equipped with lenses.

SQ displays a positioning error function in curious (dark) blue in Fig. 10 that confirms the data of Table 2. Across both receivers, *SQ* leads to the optimal rMSE. For the PDA36A2, *SQ* exhibits an equivalent performance to the m_R model: $p_{50} = 5.52$ cm (versus 5.59 cm), $p_{75} = 7.5$ cm (versus 7.5 cm) and $p_{90} = 9.39$ cm (versus 9.18 cm). For the PDA100A2-based receiver, *SQ* has a pronounced performance gain e.g. in terms of p_{90}: a 45.36 cm (83.1%) gain

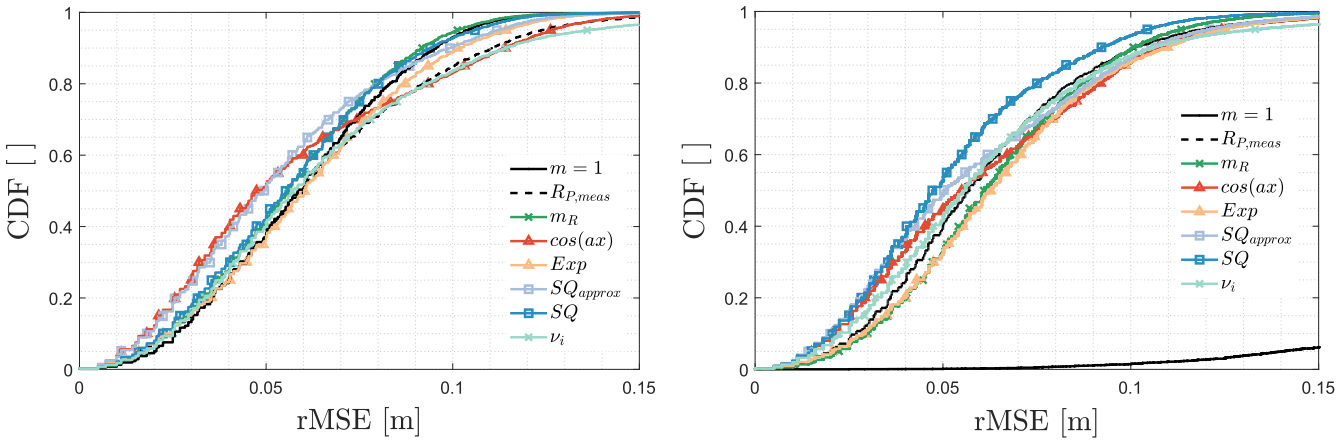

(a) PDA36A2 (b) PDA100A2

FIGURE 10. Cumulative distribution function of the rMSE found when MBF localising with the defined $R_P(\psi)$ models.

TABLE 4. rMSE [cm] for MBF positioning with the $R_P(\psi)$ models.

PDA	Percentile	$m = 1$	m_R	$cos(ax)$	Exp	SQ_{approx}	SQ	Point R_P	ν_i
36A2	50	5.85	5.59	4.74	6.02	4.95	5.52	6.02	5.7
	75	7.83	7.5	8.32	8.14	7.21	7.5	8.51	8.52
	90	9.55	9.18	11.4	10.12	9.92	9.39	11.05	11.41
100A2	50	33.97	6.08	5.5	6.26	5.02	4.72	5.7	5.59
	75	44.29	8.14	8.54	8.49	8.25	6.8	7.81	7.91
	90	54.58	10.06	10.74	10.98	10.55	9.22	10.12	10.61

over the Lambertian $m = 1$ and a 0.84 cm (8.4%) gain of the generalised Lambertian m_R.

Approximating SQ to SQ_{approx} curtails some of the positioning rMSE gain, particularly for higher percentiles ($> 75\%$). SQ_{approx}'s CDF resembles the scaled cosine $\cos(ax)$ model's. It dips below the m_R's up to approximately the 60th percentile. It even beats SQ, but solely for the PDA36A2 in the sub-60% range. Beyond 60%, SQ_{approx}'s rMSE rises more rapidly than the rMSE of m_R and SQ. The dashed line represents the positioning performance, when MBF uses the measured *Point* $R_P(\psi)$ data directly (i.e. a lookup table). It serves as a reference. Finally, Fig. 10 also shows that the ν_i fit not necessarily performs better than SQ. In fact, well-modelling $R_P(\psi)$ should obsolete the need for calibration fitting (see hereinbelow).

As a general conclusion, highly-accurate localisation really requires incorporating a well-designed $R_P(\psi)$ model i.e. the $m = 1$ model simply does not perform well enough. Of the models considered, SQ scores best in both its aptitude to model the measured $R_P(\psi)$ and its associated positioning performance.

b: MBF AND THE CALIBRATING FITS

Section III-B1 finishes by revisiting the calibrating fits of Section III-A3. Fig. 11 displays the MBF rMSE CDF for the 5 fitted propagation models, as well as the CDF of SQ and $\nu_i' = 1$, *Lamb*. $\nu_i' = 1$ represents the model with $\nu_i' = 1$ and $R_E(\phi, \gamma)$ the tabulated radiation pattern, while $\nu_i' = 1$, *Lamb* denotes the propagation model where $\nu_i' = 1$ and $R_E(\phi, \gamma)$ is approximated by the best-fitting Lambertian (i.e. with order $m = 1.138$). Comparing with the baseline $\nu_i' = 1$ shown in black, the dotted line of $\nu_i' = 1$, *Lamb* demonstrates the for the PDA36A2 substantial added error cost when the Lambertian radiation pattern is employed. The comparison hints at one of the strengths of MBF, which is that it can easily account for non-Lambertian $R_E(\phi, \gamma)$.

The subsequent models all rely on a Lambertian radiator. ν_i and ν_i tilt have a comparable positioning error, exceeding the *Power* and $\nu_i = \nu$. Interestingly, the latter models equalled or exceeded their mean R^2 values. ν_i improves upon $\nu_i' = 1$, *Lamb* at the cost of additional rMSE outliers (from the 93th percentile on). ν_i's rMSE is in the same ball park as SQ's in 50th of the grid points. ν_i also ensures a relatively accurate localisation for the PDA100A2. As a general conclusion, SQ outperforms the calibrating fits. The fits even exhibit a performance decrease compared to the baseline ν_i' due to the Lambertian approximation and overfitting on $I_{PD,i}$ -d_i.

2) 2D AND 3D TRILATERATION

a: 2D TRILATERATION

In contrast to the *fits* of the previous paragraph, not all $R_P(\psi)$ models are directly invertible for use in trilateration. The Lambertian transmitter-based propagation models associated with $m = 1$, m_R, ν_i and $\nu_i = \nu$ are readily inverted. Their 2D trilateration CDF (on tilt compensated data) is plotted in black, eucalyptus (dark) green, red and orange respectively in Fig. 12. The m_R and SQ MBF plots are repeated in green grey and white lilac for comparison. For completeness,

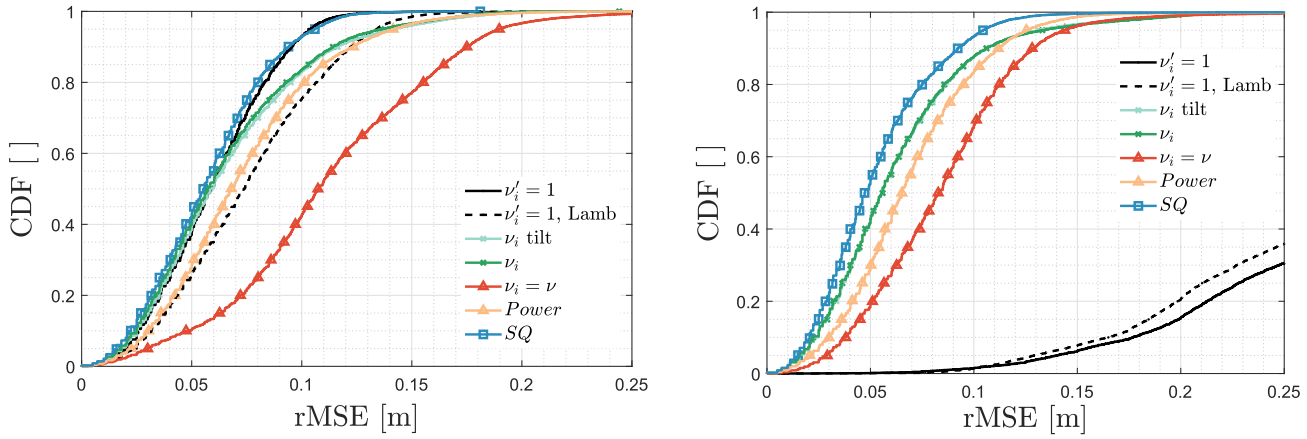

(a) PDA36A2 (b) PDA100A2

FIGURE 11. Cumulative distribution function of MBF's rMSE when employing the calibrated fit models.

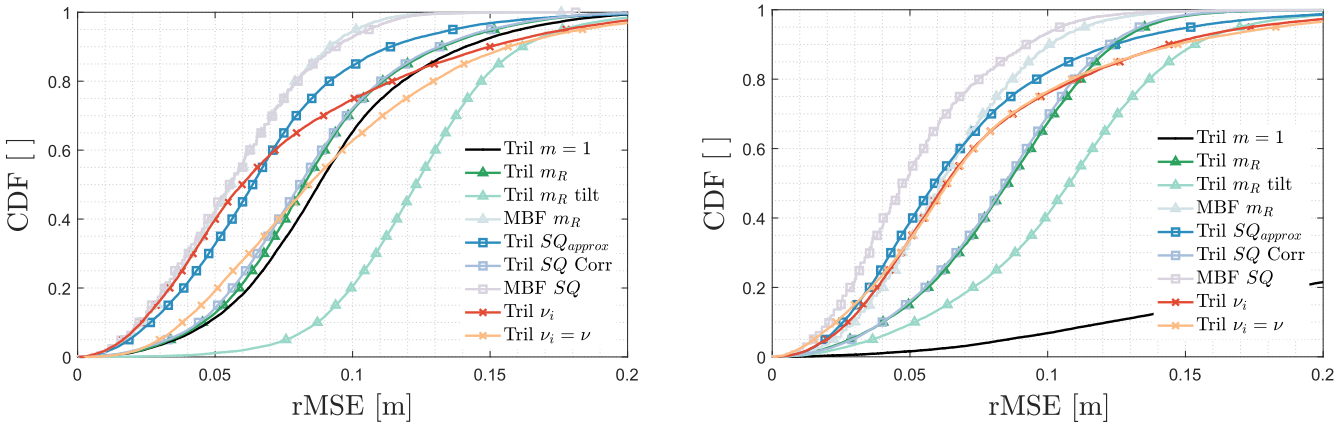

(a) PDA36A2 (b) PDA100A2

FIGURE 12. 2D Trilateration (and MBF)-based CDF's with an emphasis on (a) the PDA36A2 and (b) the PDA100A2.

'm_R tilt' shows the CDF curve that would result from effectuating trilateration with the m_R $R_P(\psi)$-based on the non-tilt-compensated dataset as well. Comparing 'm_R tilt' to m_R allows to conclude on the importance of the tilt correction.

ν_i obviously outperforms $\nu_i = \nu$ due to it fitting an exponent per LED. As both fit all available measurement data, $\nu_i = \nu$ is deemed impractical. ν_i outscores m_R in approximately 75% of the grid points, though at the cost of more exuberant outliers.

As a rule, trilateration-based VLP performs inferior to its MBF variant. Some use-cases e.g. those requiring low latency and/or a high positioning estimate update rate, do necessitate the use of trilateration. 3D-drone positioning is a prime example. Improving trilateration-based VLP is hence of paramount importance. This paper considers two potential approaches: *Tril SQ Corr* and *Tril* SQ_{approx}. The 2D positioning results of which are illustrated in the two darker blue shades.

Tril SQ Corr entails running m_R-based trilateration. The obtained position estimate is then translated into $\{\psi\}$, the set of incidence angles at the estimated position. New incidence angles $\{\psi'\}$ are searched for which (5) equals $\cos^{m_R}(\psi)$ i.e. by solving a quadratic equation. The associated *SQ* $R_P(\psi')$ is then used to recompute the PD-LED distance d_i'. This approach should enable trilateration-based VLP with an arbitrary $R_P(\psi)$ model (which could even be given by means of a Lookup table). *Tril SQ Corr* improves m_R's rMSE but a little bit, and is (in its current form) not required the additional effort. An iterative extension is part of the future work.

Tril SQ_{approx} on the other hand starts from the SQ_{approx} acceptance model. Solving for d_i delivers:

$$d_i^{3+m} = \epsilon \cdot [d_i \cdot (1 - 2\zeta) + 2\zeta\, h]\,,$$
$$\epsilon = \frac{A_R\, P_{t,i}\, h^m \cdot (m+1)}{2\pi\, P_{R,i}} \quad \text{and } \zeta = \frac{\sqrt{2}-1}{\sqrt{2}\,\psi_{3dB}^2} \tag{8}$$

with h the perpendicular distance between the LED and receiver plane. (8) can be iteratively solved. For most LEDs, the best fitting Lambertian has an order close to 1. By rounding, the d_i^{3+m}'s exponent (i.e. $3 + m$) to 4, the resulting (8) becomes a soluble quartic polynomial (of which basic solution equations are available). The *Tril* SQ_{approx} rivals the positioning performance of ν_i and can be considered the

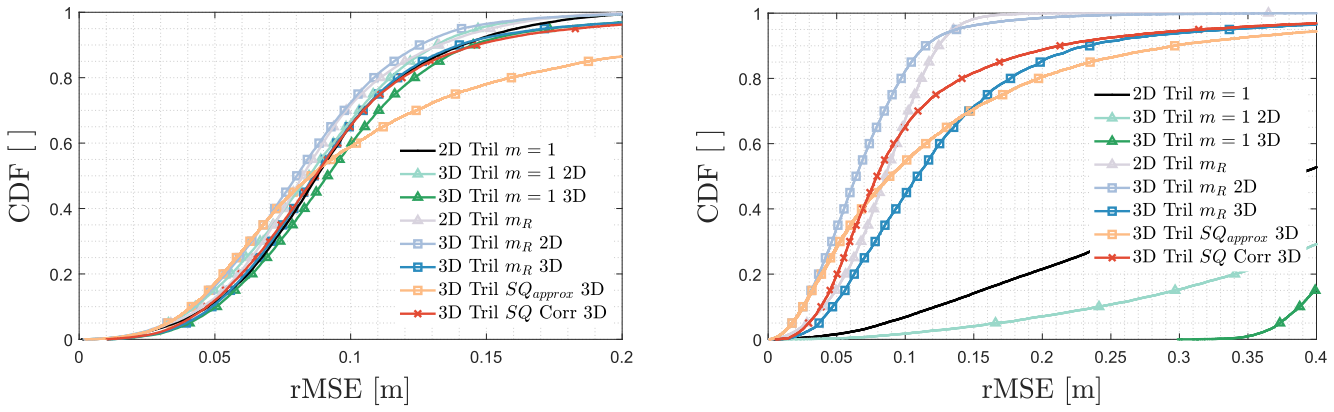

(a) PDA36A2 (b) PDA100A2

FIGURE 13. 3D Trilateration (and MBF)-based CDF's with an emphasis on (a) the PDA36A2 and (b) the PDA100A2. The first 2 letters in the legend refer to whether the 2D or 3D rMSE is reported.

best-working trilateration approach (for the LEDs under consideration).

b: 3D TRILATERATION

Fig. 13 extends the previous analysis to 3D positioning. The investigated height range Δh is limited to [2 m, 4 m] (in steps of 2.5 cm) as to account for the height ambiguity of 3D trilateration in the presence of a square-like LED constellation [16]. Fig. 13 shows the rMSE for the 2D and 3D trilateration-based algorithms. In addition, in 3D trilateration, a distinction is made between the 2D rMSE (only computing the rMSE over the x- and y-estimates) and the 3D rMSE (also accounting for the error on the receiver height estimation).

For the PDA36A2, *SQ Corr* scores equivalently to m_R, both exceeding $m = 1$'s performance for at least 90$^{\text{th}}$ percent of the grid points. SQ_{approx} works superior for around 50% of the grid locations, before the gradient of its CDF stagnates due to the distortion incurred by rounding the exponent (underestimating the LED-PD distance). After all, SQ_{approx} is designed to operate with Lambertian radiators with a unitary Lambertian order. Interestingly, when combining $m = 1$ and m_R with 3D trilateration, the p_{50} 2D rMSE values decrease by 3 mm and 2 mm respectively, compared to when 2D trilateration would be employed i.e. 3D trilateration corrects (part) of the $R_P(\psi)$ bias by incurring a height estimation error. For *SQ Corr* and SQ_{approx}, this is not the case. In the PDA100A2's case, *SQ Corr* exceedingly outperforms the other $R_P(\psi)$. $m = 1$ scores disastrously. 3D trilateration's p_{50} 2D rMSE shaves more than 2 cm off, from the p_{50} of m_R and *SQ Corr* during 2D trilateration.

As a conclusion, adequately modelling $R_P(\psi)$ is of uttermost importance in RSS-based VLP, even for trilateration that precludes non-invertible $R_P(\psi)$ models. *SQ Corr* outperforms the other $R_P(\psi)$ models for an arbitrary receiver.

C. INFLUENCE OF THE SHAPE OF THE $R_P(\psi)$ MODEL

Sections III-B1 and III-B2 proved the importance of adequately modelling $R_P(\psi)$ to deliver accurate positioning estimates. Through numerical simulation, this part is dedicated to studying the impact of the shape of the $R_P(\psi)$, and of the FOV $|\psi_C|$, of a (hypothetical) PD on the 2D MBF positioning accuracy. 8 $R_P(\psi)$ shapes are considered: (1)-(3) the m_R model of Section III-A2 with order $m_R = 1$, 3 and 5 (depicted in the green shades), (4) the *SQ* model with $\psi_{3dB} = \sqrt{\psi_C^2 \cdot \left(\sqrt{2}-1\right)/\sqrt{2}}$ (depicted in black), (5) a rectangular $R_P(\psi)$ that differs from 0 for $\psi < |\psi_C|$ as would be obtained by flattening optics (depicted in curious/dark blue), (6) a triangular $R_P(\psi) = 1 - |\psi|/|\psi_C|$ (depicted in light steel (middle) blue), (7) a Gaussian $R_P(\psi)$ with $\sigma = |\psi_C|/3$ and (8) a Laplacian $R_P(\psi)$ with diversity $b = |\psi_C|/3$. Each $R_P(\psi)$ shape is visualised in Fig. 14.

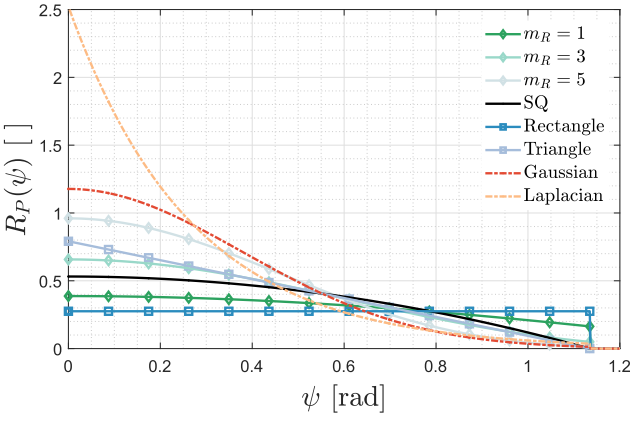

FIGURE 14. Illustration of the 8 $R_P(\psi)$ models, depicting the $R_P(\psi)$ magnitude in function of ψ for $|\psi_C| = 65°$.

The 8 $R_P(\psi)$'s associated positioning CDFs are simulated for the PDA36A2 in the idealised, virtualised VLP lab i.e. with the Lambertian LEDs (with $m = 1.138$) found at the coordinates displayed in Fig. 3 and with no LED tilt present. $|\psi_C|$ is set to either 65° or 90°, with $R_P(\psi) = 0$, $\psi \geq |\psi_C|$. $R_P(\psi)$ is normalised to 1, regardless of $|\psi_C|$. 2 receiver plane heights are considered: the ground plane (with receiver height $h_{rec} = 0$ m) and $h_{rec} = 1.5$ m above the ground plane. Furthermore, in the simulation the following

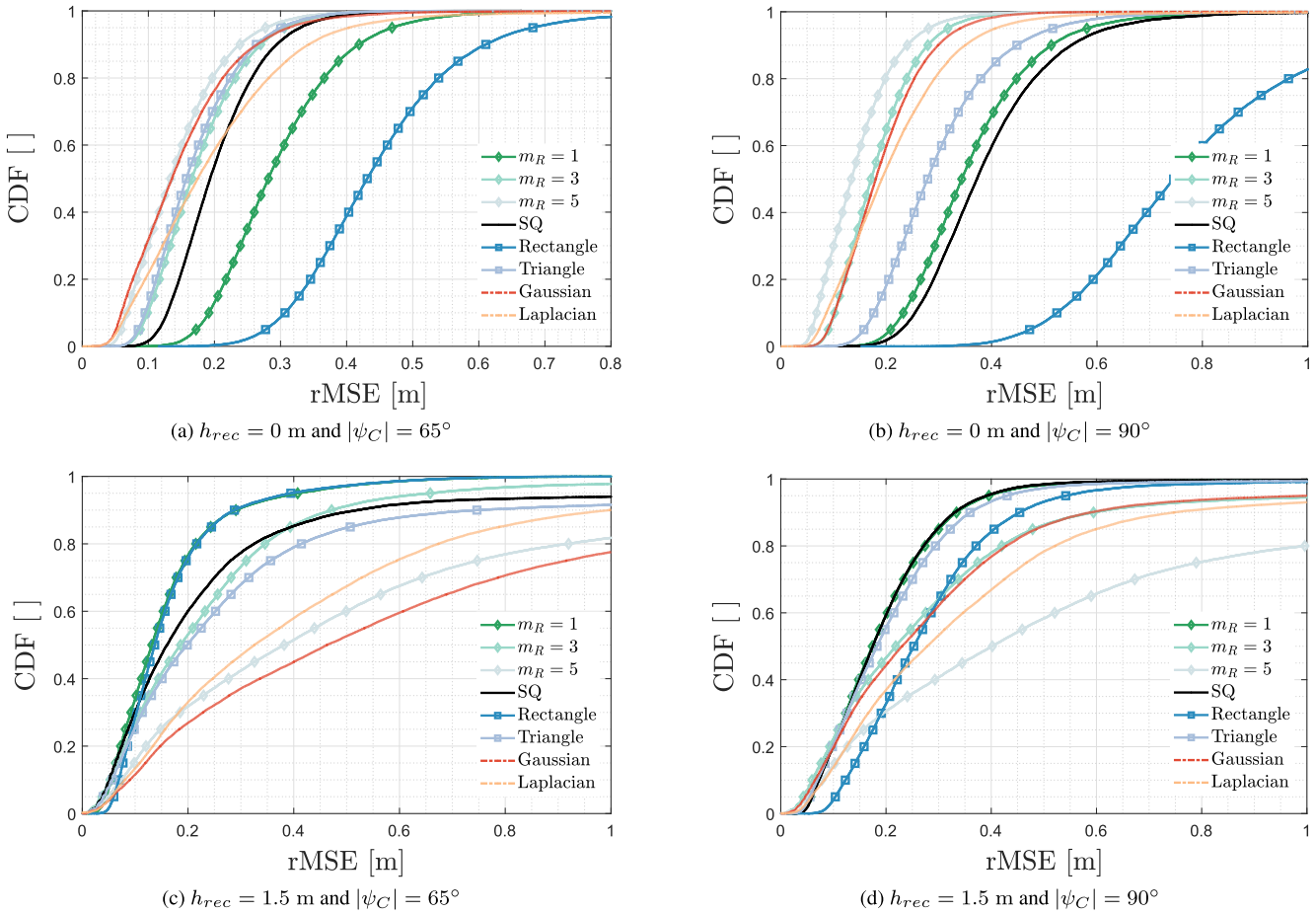

(a) $h_{rec} = 0$ m and $|\psi_C| = 65°$

(b) $h_{rec} = 0$ m and $|\psi_C| = 90°$

(c) $h_{rec} = 1.5$ m and $|\psi_C| = 65°$

(d) $h_{rec} = 1.5$ m and $|\psi_C| = 90°$

FIGURE 15. CDFs of the positioning rMSE for the 8 $R_P(\psi)$ shapes in various receiver height and field of view conditions.

applies: $M \cdot P_{t,i} \cdot \mathbf{R_P}(0) = 4$ A, the Gaussian root mean square input-referred current magnitude σ amounts to 50 nA and per 2.5 cm-spread grid point 10 $I_{PD,i}$ measurements are averaged.

Fig. 15 depicts the associated cumulative distribution of the MBF rMSE. Identifying the optimal $R_P(\psi)$ shape is far from straightforward due to the dependence on h_{rec} (thus the typical ψ found) and $|\psi_C|$. Let us consider (5) the ψ-flat rectangular shape for instance. While at $h_{rec} = 0$ m, the performance is immensely underwhelming (a p_{90} of 61.06 cm and 1.15 m for $|\psi_C| = 65°$ and $|\psi_C| = 90°$ respectively), at $h_{rec} = 1.5$ m it is able to ensure accurate localisation (highlighted by a p_{90} of 28.77 cm and 45.43 cm for $|\psi_C| = 65°$ and $|\psi_C| = 90°$ respectively). There is no need for designing complicated lens arrangements to effectuate e.g. the Laplacian behaviour, an m_R shape should generally suffice. An increasing h_{rec} demands a lower m_R for optimal performance. In conclusion, per use case, an optimal $R_P(\psi)$ can be designed/chosen depending on the gradient of $R_P(\psi)$ in the found ψ range, but this choice will not be generalizable to other environments, let alone for 3D positioning.

Fig. 16 also shows the influence of $|\psi_C|$ on $m_R = 1$. Above a critical $|\psi_C|$, which is determined by the LED type and arrangement, limiting (and normalising) the $|\psi_C|$,

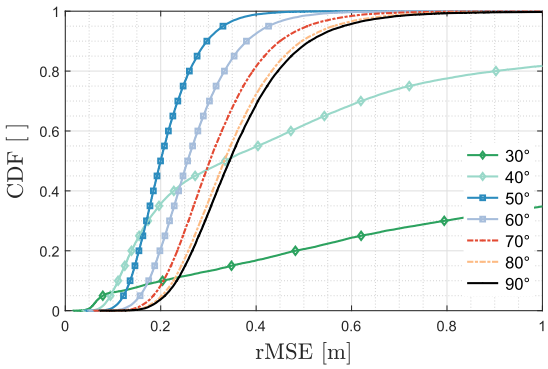

FIGURE 16. Influence of the field of view $|\psi_C| = 30 \ldots 90°$ on $m_R = 1$'s rMSE distribution at $h_{rec} = 0$ m.

increases the positioning performance. For example, when $|\psi_C|$ reduces from 60° to 50°, the p_{90} rMSE drops from 37.96 cm to 29.66 cm. When $|\psi_C|$ is limited, not rescaled, a lower $|\psi_C|$ does not necessarily translate in performance benefits i.e. unless limiting $|\psi_C|$ decreases the interference and noise contribution of other (ambient) light sources.

IV. CONCLUSION AND FUTURE WORK

This work investigates the influence of a photodiode (PD) receiver's angular dependence $R_P(\psi)$ on the relation

between the photocurrent contribution $I_{PD,i}$ and the receiver-transmitter distance d_i. Whereas in literature RSS-based VLP systems are only able to ensure accurate localisation through (arbitrarily) fitting $I_{PD,i} - d_i$ per LED, this paper shows that adequately modelling $R_P(\psi)$ via SQ, a proposed function of the square of the incidence angle ψ rather than its cosine, obsoletes this calibrating fit. Incorporating SQ in model-based fingerprinting, improves the p_{90} by 45.36 cm (83.1%) and 0.84 cm (8.4%) with respect to the ideal $m = 1$ and generalised m_R Lambertian acceptance models for the non-Lambertian-like PDA100A2 while rivalling the m_R model's score for the Lambertian-like PDA36A2. This paper also focussed on both reconciling a noninvertertible $R_P(\psi)$ with trilateration and on the (simulated) positioning performance associated with non-standard $R_P(\psi)$ characteristics.

This work provides a first step towards VLP proprietary propagation models maximising VLP's positioning potential.

The future work concentrates itself around testing more VLP receivers on the short term, and on 3D drone localisation on the longer term. While this paper focusses on photoconductive (PIN) PDs, the applicability of the $R_P(\psi)$ models and the validity of the conclusions regarding the models' associated positioning accuracy need to be verified for other PD types used in VLP e.g. for photoelectric avalanche photodiodes. During drone flight, the induced tilt necessitates a detailed $R_P(\psi)$ modelling even more. Existing algorithms will be exerted for accurate positioning in the presence of significant receiver tilt. An experimental comparison can be made with tilt-agnostic machine learning models as well.

ACKNOWLEDGMENT

This work was executed within LEDsTrack, a research project bringing together academic researchers and industry partners. The LEDsTrack project was co-financed by imec (iMinds) and received project support from Flanders Innovation & Entrepreneurship. This paper is an extended version of our paper, titled *New Photodiode Responsivity Model for RSS-based VLP*, published in Proceedings of Global Lifi Congress 2019. The authors would like to thank Matthias Van den Bossche for the realisation of the tilt/displacement/rotation platform and the VLP lab.

REFERENCES

[1] *Traceability Across the Value Chain, Advanced Tracking Systems*, European Commission, Brussels, Belgium, 2015, pp. 1–14.

[2] M. Beul, D. Droeschel, M. Nieuwenhuisen, J. Quenzel, S. Houben, and S. Behnke, "Fast autonomous flight in warehouses for inventory applications," *IEEE Robot. Autom. Lett.*, vol. 3, no. 4, pp. 3121–3128, Oct. 2018.

[3] Y. Zhuang, L. Hua, L. Qi, J. Yang, P. Cao, Y. Cao, Y. Wu, J. Thompson, and H. Haas, "A survey of positioning systems using visible LED lights," *IEEE Commun. Surveys Tuts.*, vol. 20, no. 3, pp. 1963–1988, 3rd Quart., 2018.

[4] J. Armstrong, Y. Sekercioglu, and A. Neild, "Visible light positioning: A roadmap for international standardization," *IEEE Commun. Mag.*, vol. 51, no. 12, pp. 68–73, Dec. 2013.

[5] J. Xu, C. Gong, and Z. Xu, "Experimental indoor visible light positioning systems with centimeter accuracy based on a commercial smartphone camera," *IEEE Photon. J.*, vol. 10, no. 6, Dec. 2018, Art. no. 7908717.

[6] Y. Nakazawa, H. Makino, K. Nishimori, D. Wakatsuki, and H. Komagata, "Indoor positioning using a high-speed, fish-eye lens-equipped camera in visible light communication," in *Proc. Int. Conf. Indoor Positioning Indoor Navigat.*, Montbéliard, France, Oct. 2013, pp. 1–8.

[7] Q. Wang, H. Luo, Q. Men, F. Zhao, X. Gao, J. Wei, Y. Zhang, and Y. Huang, "Light positioning: A high-accuracy visible light indoor positioning system based on attitude identification and propagation model," *Int. J. Distrib. Sensor Netw.*, vol. 14, pp. 1–13, 2018.

[8] B. Lin, X. Tang, Z. Ghassemlooy, C. Lin, and Y. Li, "Experimental demonstration of an indoor VLC positioning system based on OFDMA," *IEEE Photon. J.*, vol. 9, no. 2, Apr. 2017, Art. no. 7902209.

[9] H. Zheng, Z. Xu, C. Yu, and M. Gurusamy, "A 3-D high accuracy positioning system based on visible light communication with novel positioning algorithm," *Opt. Commun.*, vol. 396, pp. 160–168, Aug. 2017.

[10] F. Alam, M. T. Chew, T. Wenge, and G. S. Gupta, "An accurate visible light positioning system using regenerated fingerprint database based on calibrated propagation model," *IEEE Trans. Instrum. Meas.*, vol. 68, no. 8, pp. 2714–2723, Aug. 2019.

[11] F. Alam, N. Faulkner, M. Legg, and S. Demidenko, "Indoor visible light positioning using spring-relaxation technique in real-world setting," *IEEE Access*, vol. 7, pp. 91347–91359, 2019.

[12] H. Zhang, J. Cui, L. Feng, A. Yang, H. Lv, B. Lin, and H. Huang, "High-precision indoor visible light positioning using modified momentum back propagation neural network with sparse training point," *Sensors*, vol. 19, no. 10, p. 2324, 2019.

[13] Y. Chen, W. Guan, J. Li, and H. Song, "Indoor real-time 3-D visible light positioning system using fingerprinting and extreme learning machine," *IEEE Access*, vol. 8, pp. 13875–13886, 2020.

[14] P. Du, S. Zhang, C. Chen, H. Yang, W.-D. Zhong, R. Zhang, A. Alphones, and Y. Yang, "Experimental demonstration of 3D visible light positioning using received signal strength with low-complexity trilateration assisted by deep learning technique," *IEEE Access*, vol. 7, pp. 93986–93997, 2019.

[15] S. Bastiaens, D. Plets, L. Martens, and W. Joseph, "Response adaptive modelling for reducing the storage and computation of RSS-based VLP," in *Proc. Int. Conf. Indoor Positioning Indoor Navigat. (IPIN)*, Nantes, France, Sep. 2018, pp. 1–7.

[16] D. Plets, Y. Almadani, S. Bastiaens, M. Ijaz, L. Martens, and W. Joseph, "Efficient 3D trilateration algorithm for visible light positioning," *J. Opt.*, vol. 21, no. 5, May 2019, Art. no. 05LT01.

[17] S. Bastiaens, W. Raes, N. Stevens, W. Joseph, and D. Plets, "New photodiode responsivity model for RSS-based VLP," in *Proc. Global LIFI Congr. (GLC)*, Paris, France, Jun. 2019, pp. 1–6.

[18] J. M. Kahn and J. R. Barry, "Wireless infrared communications," *Proc. IEEE*, vol. 85, pp. 265–298, 1997.

[19] S. De Lausnay, L. De Strycker, J.-P. Goemaere, N. Stevens, and B. Nauwelaers, "A visible light positioning system using frequency division multiple access with square waves," in *Proc. 9th Int. Conf. Signal Process. Commun. Syst. (ICSPCS)*, Chengdu, China, Dec. 2015, pp. 1–7.

[20] H. Steendam, "A 3-D positioning algorithm for AOA-based VLP with an aperture-based receiver," *IEEE J. Sel. Areas Commun.*, vol. 36, no. 1, pp. 23–33, Jan. 2018.

[21] F. Miramirkhani and M. Uysal, "Channel modeling and characterization for visible light communications," *IEEE Photon. J.*, vol. 7, no. 6, Dec. 2015, Art. no. 7905616.

[22] G. Cossu, M. Presi, R. Corsini, P. Choudhury, A. M. Khalid, and E. Ciaramella, "A visible light localization aided optical wireless system," in *Proc. IEEE GLOBECOM Workshops (GC Wkshps)*, Houston, HI, USA, Dec. 2011, pp. 802–807.

[23] H.-S. Kim, D.-R. Kim, S.-H. Yang, Y.-H. Son, and S.-K. Han, "An indoor visible light communication positioning system using a RF carrier allocation technique," *J. Lightw. Technol.*, vol. 31, no. 1, pp. 134–144, Jan. 2013.

[24] W. Gu, M. Aminikashani, P. Deng, and M. Kavehrad, "Impact of multipath reflections on the performance of indoor visible light positioning systems," *J. Lightw. Technol.*, vol. 34, no. 10, pp. 2578–2587, May 15, 2016.

[25] W. Raes, L. D. Strycker, and N. Stevens, "Design and accuracy evaluation of a RSS-based visible light positioning implementation," in *Proc. 15th Workshop Positioning, Navigat. Commun. (WPNC)*, Bremen, Germany, Oct. 2018, pp. 1–5.

[26] D. Plets, S. Bastiaens, L. Martens, and W. Joseph, "An analysis of the impact of LED tilt on visible light positioning accuracy," *Electronics*, vol. 8, no. 4, p. 389, 2019.

[27] D. Plets, S. Bastiaens, N. Stevens, L. Martens, and W. Joseph, "Monte-carlo simulation of the impact of LED power uncertainty on visible light positioning accuracy," in *Proc. 11th Int. Symp. Commun. Syst., Netw. Digit. Signal Process. (CSNDSP)*, Budapest, Hungary, Jul. 2018, pp. 589–594.
[28] J. L. Gardner and F. J. Wilkinson, "Angular effects in silicon photodiode responsivity comparisons," *Metrologia*, vol. 34, no. 2, pp. 111–114, Apr. 1997.
[29] F. Plag, I. Kröger, T. Fey, F. Witt, and S. Winter, "Angular-dependent spectral responsivity-traceable measurements on optical losses in PV devices," *Prog. Photovoltaics: Res. Appl.*, vol. 26, no. 8, pp. 565–578, Aug. 2018.
[30] R. Schmidt, "Multiple emitter location and signal parameter estimation," *IEEE Trans. Antennas Propag.*, vol. 34, no. 3, pp. 276–280, Mar. 1986.
[31] C. Schinke, P. Christian Peest, J. Schmidt, R. Brendel, K. Bothe, M. R. Vogt, I. Kröger, S. Winter, A. Schirmacher, S. Lim, H. T. Nguyen, and D. MacDonald, "Uncertainty analysis for the coefficient of band-to-band absorption of crystalline silicon," *AIP Adv.*, vol. 5, no. 6, Jun. 2015, Art. no. 067168.

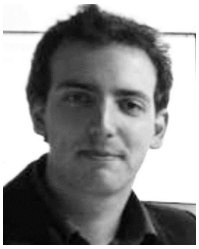

SANDER BASTIAENS received the B.Sc. and M.Sc. degrees in electrical engineering from Ghent University, in 2015 and 2017, respectively, where he is currently pursuing the Ph.D. degree in indoor location tracking using the wireless IoT technology and visible light positioning.

In 2017, he joined the WAVES Research Group, Department of Information Technology (INTEC), Ghent University/imec. His current research interests include indoor localisation and propagation, with a strong focus on industrial visible light positioning.

WILLEM RAES received the master's degree in engineering technology from KU Leuven, Belgium, in 2017, where he is currently pursuing the Ph.D. degree in engineering technology with the DRAMCO Research Group, ESAT.

Since 2017, he has been participating in multiple projects focusing on the valorisation of visible light-based indoor localisation for industry. His main research topics are visible light-based indoor localisation and electronics design.

NOBBY STEVENS (Member, IEEE) received the master's degree in physical engineering from Ghent University, Ghent, Belgium, in 1997, the D.E.A. degree from the Institut National Polytechnique de Grenoble, Grenoble, France, in 1997, and the Ph.D. degree from Ghent University, in 2004. From the end of 1997 to August 1998, he was a Product Development Engineer with Philips. Beginning in August 1998, he performed research on the numerical modeling of electromagnetic fields interacting with the human body with the Department of Information Technology, Ghent University. In June 2004, he joined Agilent EEsof, Santa Rosa, CA, USA, as a Research and Development Engineer, where he was involved in computational electromagnetics. Since November 2008, he has been performing research with the DRAMCO (wireless and mobile communications) Group, ESAT, KU Leuven, Ghent. In 2018, he was appointed as an Associate Professor at the Faculty of Engineering Technology, KU Leuven. His research interests include visible light positioning and embedded machine learning.

LUC MARTENS received the M.Sc. degree in electrical engineering from Ghent University, Belgium, in July 1986, and the Ph.D. degree, in December 1990.

From September 1986 to December 1990, he was a Research Assistant with the Department of Information Technology (INTEC), Ghent University. During this period, his scientific work was focused on the physical aspects of hyperthermic cancer therapy. His research work dealt with electromagnetic and thermal modeling and the development of measurement systems for that application. Since 1991, he has been managing the Wireless and Cable (WiCa) Research Group, INTEC. Since 2004, the WiCa Research Group has been a part of the iMinds Institute, and since April 1993, he has been a Professor with Ghent University. His experience and current interests are in modeling and measurement of electromagnetic channels, electromagnetic exposure, that is, around telecommunication networks and systems, such as cellular base station antennas, and energy consumption in wireless networks. He has authored or coauthored more than 300 publications in the domains of electromagnetic channel predictions, dosimetry, exposure systems, and health and wireless communications.

WOUT JOSEPH (Member, IEEE) was born in Ostend, Belgium, on October 21, 1977. He received the M.Sc. degree in electrical engineering from Ghent University, Belgium, in July 2000, and the Ph.D. degree, in March 2005.

From September 2000 to March 2005, he was a Research Assistant at the Department of Information Technology (INTEC), Ghent University. During this period, his scientific work was focused on electromagnetic exposure assessment. Since October 2007, he has been a Postdoctoral Fellow of the FWO-V (Research Foundation-Flanders). Since October 2009, he has been a professor in the domain of experimental characterization of wireless communication systems with Ghent University. He has been an imec PI, since 2017. His research work dealt with measuring and modeling of electromagnetic fields around base stations for mobile communications related to the health effects of the exposure to electromagnetic radiation. His professional interests are electromagnetic field exposure assessment, propagation for wireless communication systems, and antennas and its calibration. Furthermore, he specializes in wireless performance analysis and the quality of experience.

DAVID PLETS (Member, IEEE) received the M.Sc. degree in electrical engineering and the Ph.D. degree from Ghent University, Ghent, Belgium, in 2006 and 2011, respectively.

In 2016, he became a part-time Professor in exposure to multiple physical agents in smart buildings. He is currently a member of the WAVES Research Group, Department of Information Technology, Ghent University/imec. His current research interests include localization techniques and the IoT, for both industrial and health-related applications. He is also involved in research on the optimization of (cognitive) wireless communication networks, with a focus on coverage, interference, and exposure.